Response of Lanthanide Sesquioxides to High-Energy Ball Milling

Eric C. O'Quinn,* Alexandre P. Solomon, Casey Corbridge, Cale Overstreet, Cameron Tracy, Antonio F. Fuentes, David J. Sprouster, and Maik K. Lang

Sesquioxides (M_2O_3) exhibit rich polymorphism with distinct phases that form over broad compositional, pressure, and temperature ranges. This makes these materials an ideal model system for studying the effects of high-energy ball milling and the far-from-equilibrium conditions induced by complex mechanical interactions. Polycrystalline bixbyite-structured binary sesquioxides (M_2O_3, M = Gd, Dy, Ho, Er, Yb, and Y) were processed by high-energy ball milling and the resulting structural modifications were characterized by synchrotron X-ray diffraction. Ball milling drives the initial cubic structure ("C-type") in each oxide to the monoclinic, "B-type" structure, with the rate of formation and maximum attainable phase fraction dependent on the cation size. The B-type phase fraction increases with milling time for each sesquioxide, but reaches steady-state behavior below unity, which contrasts with previous studies that induced a complete transformation by exposure to temperature, pressure, or ion radiation. This behavior suggests a complex interaction regime within a planetary ball mill characterized by transient processes, which exert simultaneous 1) driving forces to form the B-type phase and 2) kinetic pathways to partially recover the C-type phase. We show that these two processes are correlated with the effects of pressure and temperature during mechanical interactions between the sample and milling tools.

1. Introduction

Mechanochemistry is a branch of physical chemistry that involves the manipulation and/or transformation of substances

by the deposition of mechanical energy.[1–3] The primary tool of mechanochemistry is a *ball mill,* a rotating closed container in which balls are placed along with the substance of interest, typically a powder.[4] The physics of ball–sample interactions is complex, and many different models have been developed to explain it. Most popular theories for mechanochemical reactivity, such as the magma-plasma theory[5] and the hot-spot model,[6] predominantly involve localized, short-lived, high-temperature, and high-pressure non-equilibrium states.

However, it is widely recognized that the aforementioned models, individually, do not offer a comprehensive explanation for the wide range of physical and chemical processes observed under continuous mechanical energy input. Nevertheless, it is universally accepted that the activation energy, which typically inhibits the rate of atomic and molecular processes, is reduced during milling through a combination of mechanical stress and thermal energy and that the rate of such processes increases with applied stress.[2,7–9] Although the high-energy ball milling technique was originally developed to reduce and refine the grain sizes of oxide powders, this highly nonequilibrium environment produced during milling drives the material along structural transition pathways that are often not accessible by conventional near-equilibrium processing routes.[1] Oxides synthesized or processed within a mill can undergo polymorphic, order–disorder, or crystalline–amorphous transformations.[1] These transformations are highly correlated with the dynamic energy depositions induced by the milling tools and the parameters used in the milling procedure (e.g., rotational speed, processing time, and ball-to-powder ratio).

Simple oxides with the M_2O_3 stoichiometry (M = lanthanide or Y) serve as a useful model system for the study of mechanochemical processing. These materials exhibit a wide range of properties that make them important in many technologies, such as high-κ dielectrics for semiconductors,[10] nanoparticles for medical imaging,[11] and neutron absorbers for nuclear reactors.[12] Their crystallography and polymorphism were initially evaluated by Goldschmidt,[13] Zachariasen,[14] and Pauling and Shappell.[15] Goldschmidt observed that, despite the chemical similarity of the lanthanides and the relatively small variation

E. C. O'Quinn, A. P. Solomon, C. Corbridge, C. Overstreet, M. K. Lang
Department of Nuclear Engineering
University of Tennessee
Knoxville, TN 37996, USA
E-mail: ericoquinn@utk.edu

C. Tracy
Center for International Security and Cooperation
Stanford University
Stanford, CA 94305, USA

A. F. Fuentes
Cinvestav Unidad Saltillo
25900 Ramos Arizpe, Coahuila, Mexico

D. J. Sprouster
Department of Materials Science and Chemical Engineering
Stony Brook University
Stony Brook, NY 11784, USA

in ionic radius across lanthanide cation series ("lanthanide contraction," from 1.03 Å for La to 0.86 Å for Lu), lanthanide sesquioxides exhibit three distinct structures under ambient conditions (**Figure 1**); Goldschmidt's designators for the structures, "A," "B," and "C," are still widely used today. M_2O_3 oxides with large cations (La – Nd) adopt the trigonal "A-type" structure, P-$3m1$, while those with small cations (Tb – Lu, Y) adopt the cubic "C-type" structure, Ia-3, which is isostructural with the mineral bixbyite. Sesquioxides with intermediate-sized cations (Pm - Gd) can adopt the monoclinic "B-type," $C2/m$, or the cubic C-type structures.[16,17] At high temperatures, the hexagonal "H-type" polymorph, $P6_3/mmc$, is accessible for many of these sesquioxides, as well as the cubic "X-type" polymorph, Im-$3m$.

The C-type structure is a derivative of its parent MO_2 fluorite structure, Fm-$3m$. The fluorite structure is characterized by interpenetrating arrays of cations (face-centered cubic) and anions (simple cubic), which form dense planes along the [111] direction of the alternating sequence: anions–cations–anions.[18] Both cation and anion layers are fully dense configurations described by triangular Ising nets,[19] and the cations are in ideal cubic, eightfold coordination with the anions. The cubic, C-type structure, like fluorite, exhibits a layered structure of cations and anions, with the cation layers forming dense triangular nets. However, the anion layers contain constitutional vacancies in specific clusters that resemble a "wishbone".[20] The presence of intrinsic vacancies results in relaxations of some of the cations and all the anions away from an ideal fluorite lattice; the $24d$ cations relax along [100], while the anions ($48e$) are free to relax in all directions. The arrangement of vacancies also reduces the coordination of the cations from eight in fluorite to six in the C-type structure. The monoclinic, B-type structure, unlike the C-type phase, is characterized by fully dense triangular nets on both cation and anion sublattices which form the sequence: anions–cations–anions–cations–anions.[20] This yields one cation site that has sixfold octahedral coordination and two cation sites that have sevenfold coordination within a square face-capped trigonal prism. Finally, the trigonal, A-type structure is similar to the B-type phase in that both cation and anion sublattices are fully dense triangular nets, but the sequential stacking of these nets is anions–cations–anions–anions–cations. In the A-type structure, all cations are in sevenfold coordination within face-capped octahedra. Accordingly, the B → A phase transition is considered *displacive*, whereas C → B and C → A, are both considered *reconstructive*.

In addition to varying the cationic radius, the polymorphism of sesquioxides can be accessed through the application of temperature and/or pressure. Early studies by Foex, Traverse, and Coutures[21–23] demonstrated the high-temperature phase diagram for these sesquioxides. Cubic (C-type) sesquioxides with smaller cations do not transform to the monoclinic (B-type) phase at high temperature: Lu_2O_3 remains cubic up to the melting point, while Yb_2O_3, Tm_2O_3, and Er_2O_3 transform to the hexagonal (H-type) phase before melting. Those with medium-sized cations (A = Pm-Ho) transform to the B-type phase at high temperature with a transition temperature that correlates negatively with ionic radius. The C-to-B-type transformation is reversible for all of these sesquioxides.[24] Although a subset of these sesquioxides (M = Pm-Gd) undergoes a B-to-A-type transformation at higher temperatures, they eventually transform to the H-type phase. Finally, for sesquioxides with M = Pm-Dy, the H-type transforms to the cubic, X-type phase before melting; Ho_2O_3 directly melts from the H-type phase. Hoekstra[25] was the first to probe the high-pressure behavior of these sesquioxides and revealed that, unlike for temperature, the B-type phase can be accessed at high pressures for all C-type sesquioxides, even those with small cations that do not transform to the B-type phase under high temperatures. This is because the C-to-B-type transformation is associated with a volume contraction (≈8%) which increases the stability of the B-type phase relative to the C-type phase under the application of pressure.[24,25] Hoekstra showed that the critical pressure for the C-to-B-type transformation is negatively correlated with the cationic radius and that the transformation is reversible.[25]

Inducing phase transitions in the C-type sesquioxides is also possible through processing with far-from-equilibrium conditions. For example, heavy ion irradiation[26,27] drives a variety of phase transitions in M_2O_3 sesquioxides, which are highly correlated with the cationic radius, as well as the ion species and the energy deposition profile.[26–31] For instance, Tracy et al.[27] demonstrated that irradiation with 2.25 GeV Au ions induces the C-to-B-type transition in sesquioxides with medium-sized cations (M = Sm, Gd, Ho) via extreme ionizations, but not in sesquioxides with smaller cations (M = Tm and Lu). Intriguingly, after exposure to 185 MeV Xe ions, producing higher local energy densities, the former group became amorphous, while the latter underwent a C-to-X-type transformation. There is, by contrast, much less literature on the effects of high-energy ball milling, another far-from-equilibrium processing technique.[32] It has been shown that Dy_2O_3 and Yb_2O_3 undergo the C-to-B-type phase transition during milling with steel tools,[1,17,33] while Er_2O_3 is amorphizable. It was suggested that this milling-induced phase transition may be a critical precursor step when synthesizing complex oxides such as Ln_2TiO_5 and $Ln_2Ti_2O_7$
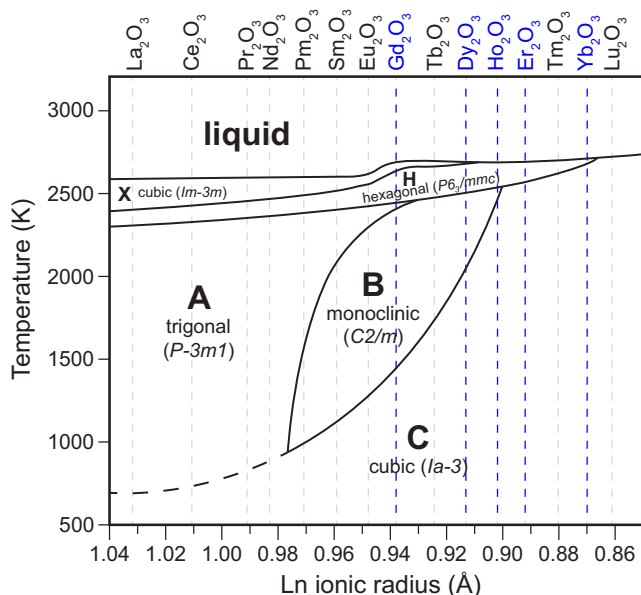
Figure 1. High-temperature phase diagram of Ln_2O_3 sesquioxides adapted from Coutures et al.[22] The oxides examined in this study are highlighted in blue.

ADVANCED
SCIENCE NEWS
www.advancedsciencenews.com

ADVANCED
ENGINEERING
MATERIALS
www.aem-journal.com

(Ln = lanthanide) by mechanochemical means using yttria-stabilized zirconia tools.[34,35]

Mechanochemical processes are complex due to varying strain, temperature, and pressure conditions which makes assessment of the underlying physics complex. However, comparing and contrasting results from multiple far-from-equilibrium processes, such as ion irradiation and high-energy ball milling, on the same materials can provide more fundamental insights into both the mechanisms of mechanochemical transformations and the nature of the extreme environments present in a ball mill. In this study, we systematically processed six C-type sesquioxides in a planetary ball mill equipped with tungsten carbide (WC) tools and analyzed their structural responses using synchrotron X-ray diffraction (XRD). Each M_2O_3 compound (M = Gd, Dy, Ho, Er, Yb, and Y) underwent a C-to-B-type transition after milling with the accumulation rate and final B-type phase fraction depending greatly on the cation of the sesquioxide (ranging from 0.94 to 0.87 Å) and the milling time.

2. Experimental Section

Polycrystalline powders of M_2O_3 materials (M = Gd, Dy, Ho, Er, Yb, and Y) were purchased from Alfa Aesar, with purities of >99.99% and a grain size on the order of 1 μm. Materials were milled without solvents and in an ambient environment in a Retsch PM200 planetary ball mill operating with a sun wheel rotational speed of 350 rpm and speed ratio of 1:-2 (sun wheel: vial). Typically, two sesquioxide samples were milled simultaneously using two 125 mL WC jars and ≈8.2 g WC balls (10 mm diameter) such that the ball-to-sample mass ratio was 12:1. The sampling of the milled powder was conducted within the first hour, at intervals of 1, 5, 15, 30, 45, and 60 min. Subsequently, every 15 min, the mill would stop for one minute before reversing direction and continuing. Every three hours, the mill was stopped, any accumulated powder on the walls was scraped, and the entire sample was manually homogenized in a mortar. Generally, samples were collected every 3 h until completing 24 h of milling. After each extraction step, the number of balls was adjusted to maintain a consistent ball-to-sample mass ratio of 12:1 throughout the entire milling operation.

Samples were characterized after milling using synchrotron-based XRD. Angle-dispersive XRD was performed using beamline 16-BM-D (HPCAT sector) of the Advanced Photon Source at Argonne National Laboratory. X-rays with 30 keV were used in transmission geometry and a 5 × 4 μm beam spot to probe the milled samples placed in cylindrical molybdenum chambers of 100 μm diameter and 25 μm thickness. The details of this measurement setup can be found elsewhere.[36] Debye rings were collected on a Mar345 image plate detector calibrated with a NIST CeO_2 calibrant, with a nominal sample-to-detector distance of 318 mm and an X-ray wavelength of 0.4133 Å, and two-dimensional diffraction images were integrated into one-dimensional X-ray patterns using Dioptas.[37]

In situ high-temperature XRD was performed up to 1200 °C at the X-ray powder diffraction beamline of the National Synchrotron Light Source II at Brookhaven National Laboratory, to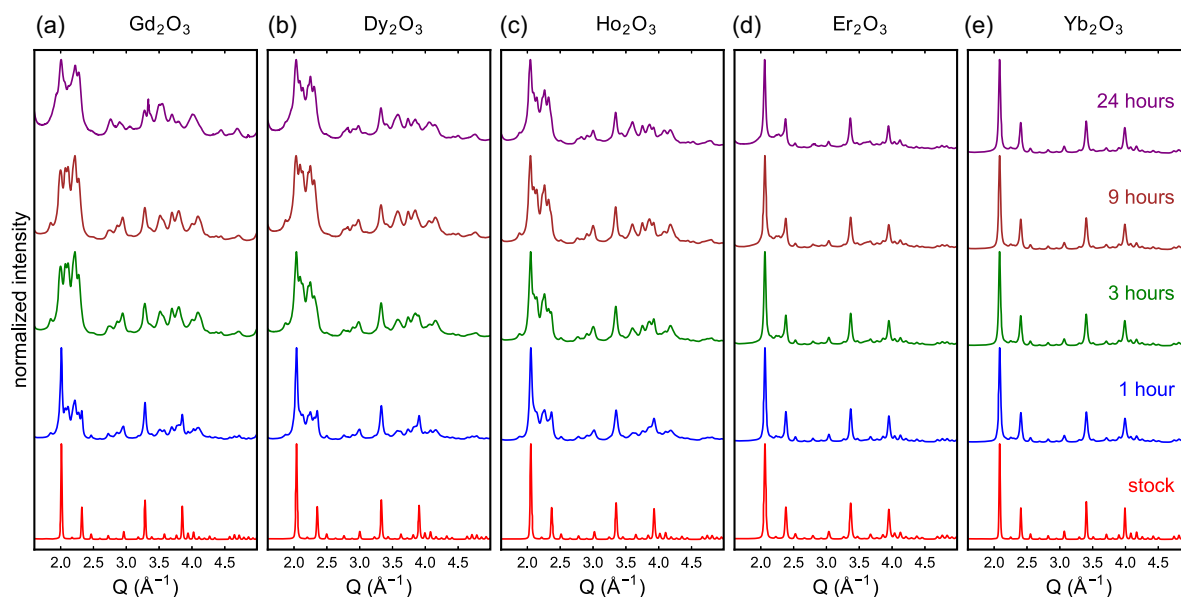 thermally anneal samples transformed by planetary ball milling. Samples were heated using a hexapole lamp furnace setup with halogen lamps focused onto the sample position. Milled M_2O_3 (M = Gd, Dy, Ho, Er, Yb, and Y) samples were loaded into 2 mm diameter quartz capillaries with 0.1 mm wall thickness. The capillaries were inserted horizontally into the lamp furnace and aligned using a laser. X-rays with 67 keV scattered from the sample and were recorded with a PerkinElmer XRD 1621 digital imaging detector. NIST LaB_6 and CeO_2 standards were used for instrument parameter calibration for ambient and high-temperature measurements, with a nominal sample-to-detector distance of 1429.84 mm and an X-ray wavelength of 0.1846 Å. The temperature inside the chamber was determined using the thermal expansion of a CeO_2 standard and correlated with the adjusted lamp power. Samples were measured separately at various temperatures (25–1200 °C). Subsequent temperature steps were reached using a heating rate of 5 °C min^{-1} and the samples were allowed to equilibrate for 30 s before two-minute measurements were performed, to achieve high signal-to-noise ratios. Two-dimensional images were integrated into one-dimensional patterns using PyFai.[38] The GSAS-II software was utilized for image calibration and integration.[39]

Rietveld refinement[40] of XRD patterns was performed to analyze all structural changes induced by the milling of sesquioxide samples. XRD patterns were refined to cubic (C-type) and monoclinic (B-type) structures, or a combination of both structural models. The refined parameters included the global scale, phase fractions, unit cell parameters ($a = b = c$ for C-type and $a \neq b \neq c$, $\beta \neq 90°$ for B-type), microstrain, and symmetry-constrained atomic positions. To limit the number of free parameters, a global isotropic atomic displacement parameter was applied to all atoms. To address peak intensity variations observed in some samples with the B-type phase, the March–Dollase[41,42] model was applied to account for apparent preferential orientation along the (310) planes.

3. Results and Discussion

XRD patterns (**Figure 2**) reveal phase-pure and well-crystallized starting samples all exhibiting the cubic C-type structure. The patterns of the samples after milling exhibit additional peaks that grow in intensity with increasing milling time at the expense of C-type peak intensities. The additional peaks are more pronounced for the sesquioxides with larger cations (e.g., Gd_2O_3) and less so for the sesquioxides with smaller cations (e.g., Yb_2O_3), which can be clearly observed for the patterns of all samples after milling for one hour (**Figure 3**a). In all patterns, these peaks are consistent with the monoclinic B-type structure.

The patterns were further examined by Rietveld refinement. For this, a two-phase model of variable monoclinic B- and cubic C-type fractions was used to refine the XRD patterns (Figure 3b). No evidence of other phases, such as impurities from the WC grinding media, or amorphization was detected in any XRD patterns. The goodness-of-fit parameter (R_w) was below 7.2% for all refinements. All samples partially transform to the monoclinic B-type structure on milling, with a B-type phase fraction that initially increases with milling time (**Figure 4**). After one minute of milling, the shortest duration tested in this study, the B-type phase fractions ranged from 2.3% (Yb_2O_3) to 8.6% (Gd_2O_3).

**ADVANCED
SCIENCE NEWS**

www.advancedsciencenews.com

**ADVANCED
ENGINEERING
MATERIALS**

www.aem-journal.com

Figure 2. a) Representative XRD patterns of Gd_2O_3, b) Dy_2O_3, c) Ho_2O_3, d) Er_2O_3, and e) Yb_2O_3 before and after milling for labeled durations.
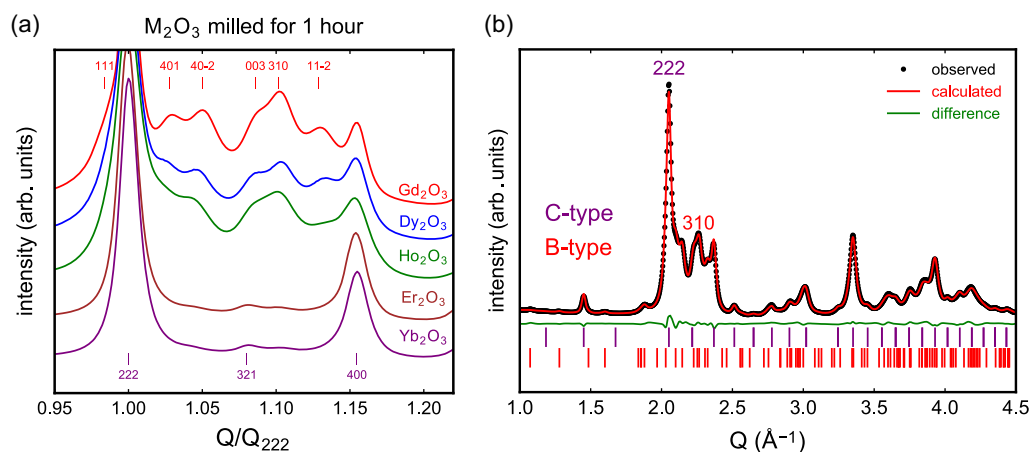

Figure 3. XRD patterns of M_2O_3 samples milled for one hour. In a) the x-axis is normalized to the position of the most intense diffraction peak, the (222) C-type peak. Bragg peaks corresponding to the C-type (purple, bottom) and B-type (red, top) phases are indexed for oxides for which the respective phase is dominating. b) Representative Rietveld refinement of the diffraction pattern of Ho_2O_3 milled for one hour. The March–Dollase ratio of the $(310)_B$ peak is 1.15, indicating disproportionate overrepresentation of intensity in these B-type planes in the diffraction pattern.

The amount of B-type phase present after a given milling time decreases across the lanthanide series, with decreasing cationic radii from Gd_2O_3 to Yb_2O_3. This effect is particularly clear in the diffraction patterns of all samples milled for 1 h (Figure 3a). For all oxides, the B-type phase fraction initially exhibits a rapid linear increase with milling time, which is followed by sublinear growth and eventual saturation below unity between 1 and 3 h of milling. In all cases, the broadening of diffraction peaks can be modeled with Rietveld refinement solely by the accumulation of microstrain, with a negligible contribution to broadening from decreasing crystallite size. Regardless, nanocrystalline sesquioxides (M = Gd-Lu) have been previously shown to adopt the C-type structure, so grain size reduction cannot be the source of the B-type transition observed here.[43,44] Consistently in all

samples, the B-type (310) reflection is the most intense diffraction maximum of the monoclinic phase (Figure 3b). This indicates potential texture effects in the milling-induced B-type phase as, for a non-textured sample, the (−112) peak should be the most intense peak for this phase.[45]

The rate at which the B-type fraction forms (the slope of the linear regime at shorter milling times) and the maximum phase fraction at which it saturates (the plateau region for longer milling times) relate directly with the size of the lanthanide cation. Qualitatively, Gd_2O_3, with the largest cation in the present series, shows the most rapid accumulation of the milled B-type phase and the highest phase fraction in the saturation regime, while the opposite is observed for Yb_2O_3, having the smallest cation. Linear fits to the B-type fractions during the first hour of milling
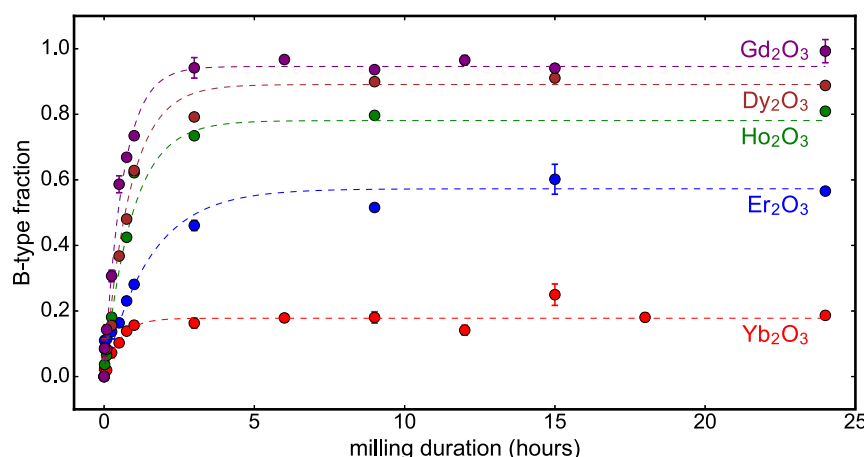
Figure 4. B-type phase fraction induced by ball milling of each compound extracted from Rietveld refinement of the XRD patterns. The dashed lines are fits of Equation (4) to each data series. Error bars represent the uncertainties of phase fractions based on Rietveld refinements.

were used to determine the initial growth rate of the milled B-type phase (**Figure 5**a). Similarly, the maximum phase fraction of the B-type phase accessible under the present milling
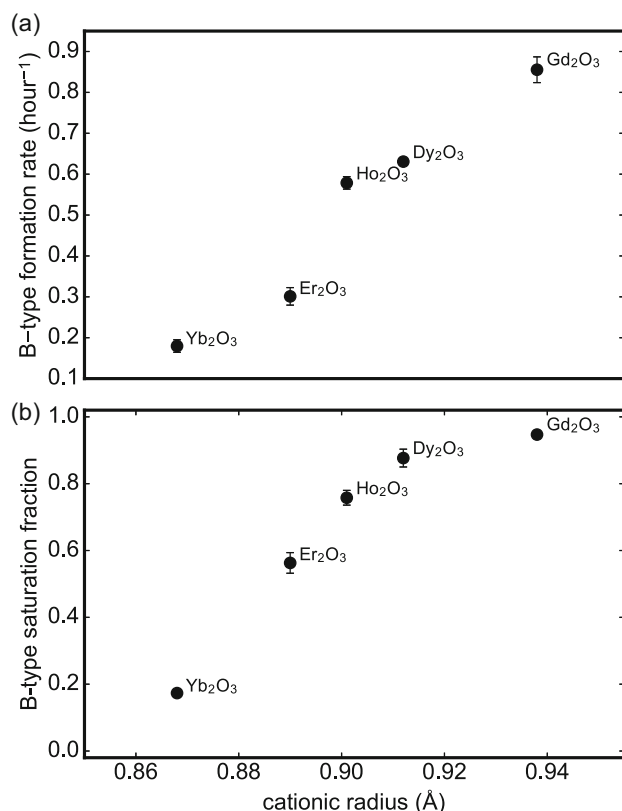
Figure 5. a) B-type formation rate and b) maximum B-type saturation fraction. The B-type formation rate was determined by a linear fit (y-intercept = 0) of the B-type phase fractions over the first hour of milling. The B-type saturation fraction was determined by a linear fit (slope = 0) of the B-type fractions for milling times greater than three hours when a steady state was reached. The error bars correspond to uncertainties in the linear fitting.

conditions was estimated by fitting horizontal lines to the B-type fractions for milling times greater than three hours (Figure 5b). The extracted values of the linear increase and saturation agree with what was qualitatively observed: they are the highest for Gd_2O_3 (86(3)%/h to 95(1)% saturation, respectively) and the lowest for Yb_2O_3 (18(2)%/h to 17(1)% saturation, respectively). Both parameters increase with the cationic radius and exhibit linear-type behavior throughout the whole range (Figure 5).

The monoclinic B-type phase is generally observed in these sesquioxides either during or after high-temperature treatment (Figure 1) and/or high-pressure exposure with critical transformation temperatures/pressures between 1152 °C (Gd_2O_3) and 2185 °C (Ho_2O_3) and 4 GPa (Gd_2O_3) and 13 GPa (Yb_2O_3).[21,22,24,46,47] The B-type phase is not observed at high temperature for Er_2O_3 or Yb_2O_3. In prior temperature and pressure experiments, it has been shown that the C-to-B-type transformation is reversible, but it can suffer from slow kinetics.[21,24,25] As with the milling results in this study (Figure 4), the fraction of B-type phase that forms under given temperature/pressure conditions is negatively correlated with the cation size across the M_2O_3 series; however, the B-type phase formation can be complete if sufficiently large temperature/pressure conditions are reached. The transition from the equilibrium C-type to the metastable B-type after high-energy milling suggests that interactions between the sample and milling tools induced high temperatures and/or high pressures; in contrast to equilibrium heating and static compression, temperature and pressure conditions must be transient with associated far-from-equilibrium energy depositions. This can be inferred from several models that have previously been established to describe the physics involved in the milling process. Rapid rises in temperature and pressure followed by fast quenching are key components of, for example, the magma-plasma theory and the hot-spot model with timescales on the order of milliseconds or faster.[2] The distinct variability in B-type phase formation across the range of lanthanide cations in sesquioxides provides an opportunity to better understand the underlying physics and accessible transient temperature/pressure regimes that occur during interactions between the sample and milling tools, particularly when

comparing and contrasting with other far-from-equilibrium processing techniques.

Oxide materials manipulated by high-energy ball milling belong, more broadly, to the larger class of "*driven materials,*"[48] referring to those processed by non-equilibrium means with some form of external forcing. For instance, exposure to ions with energies greater than ≈ 1 MeV/nucleon (known as "*swift heavy ions*"), which encompass alpha particles, galactic cosmic rays, and large atomic fragments generated by nuclear fission,[49] can also trigger polymorphic,[50] order–disorder,[51] or crystalline–amorphous transformations[52] in oxide materials. This form of highly ionizing irradiation deposits kinetic energy (up to 10s of keV per nm traveled) to the electrons of the material within an exceedingly short interaction time (less than fs), resulting in (1) excitation of electrons from the valence band into the conduction band (leaving holes in the valence band) and (2) liberation of high-energy "delta electrons" into the surrounding material matrix.[53,54] In insulators, this results in a nanometric cylindrical volume of electron–hole plasma contained within a cold, unperturbed solid matrix.[49] An extreme rise in electronic temperature changes the potential energy landscape, driving material modifications and rapid relaxation pathways.[54] Extremely high-energy densities (up to tens of eV/atom) are induced as excited electrons relax and transfer energy to phonons, resulting in complex structural modifications[27,51] which can include local melting, amorphization, and creation of metastable crystalline phases within the modified ion track.[55,56]

Under milling, the C-to-B-type transformation proceeds with a wide variation in rates (Figure 5a) from Gd_2O_3 ($\approx 15\%$ after 5 min) to Yb_2O_3 ($\approx 15\%$ after 60 min), which agrees well with B-type phase formation behavior under high-energy ion irradiation[27] in that the B-type formation rate correlates directly with cationic radii. However, one key difference in the response of these sesquioxides to milling and ion irradiation is that for sesquioxides with smaller cations (Tm_2O_3, Lu_2O_3), no B-type phase was reported under ion irradiation and formation of a high-temperature, cubic (X-type) phase was the only observed radiation response. Another difference is in the amount of maximum attainable B-type phase. For all milled samples, the fraction of the B-type phase reaches a saturation value below unity (Figure 5b), even with extended milling times. The maximum B-type phase fraction observed across all samples is about 95%, which was reached for Gd_2O_3 after 3 h of milling using a speed of 350 rpm. In contrast, exposure to swift heavy ions completely transforms the sesquioxides with larger cations (Sm_2O_3, Gd_2O_3, Ho_2O_3) to the B-type phase, if sufficiently high ion fluences are applied.[27]

For ion-beam-induced B-type phase formation (the fraction of which is given by f_B) and its accumulation with increasing ion fluence (ϕ), a Poisson-type *direct-impact transformation model* was used to describe the data[57] to account for the linear increase followed by sublinear growth and eventual saturation (in this case at 100%):

$$\frac{df_B}{d\phi} = \sigma_B(1 - f_B) \tag{1}$$

$$f_B(\phi) = 1 - e^{-\sigma_B \phi} \tag{2}$$

where the transformation rate (Equation (1)) depends only on the cross-sectional area of transformation per incoming ion (σ_B) and the amount of untransformed sample remaining ($1 - f_B$) at a given ion fluence. Each ion transforms C-type into the B-type within σ_B and the B-type phase initially grows linearly with fluence until ion tracks start to overlap and the increase in B-type phase fraction slows. The entire sample is eventually transformed at very high fluences.[27] The complete transformation for ion irradiation implies that the ion-track structure is simple consisting only of B-type phase without additional "shell" or "halo" regions of distinct structural modifications, as reported for other oxides.[58] The overall accumulation process of the milled B-type phase has a very similar initial linear behavior, sublinear regime, and eventual saturation, but the transformation remains incomplete (Figure 5b). This implies that some recovery processes are active during or in between sample-tool interactions that convert a fraction of the B-type phase back to C-type with a rate that increases as the cationic radius decreases (Figure 5b).

A similar Poisson-like accumulation model was applied to describe the B-type phase accumulation after ball milling as a function of milling time instead of ion fluence as for irradiation; however, Equation (1) and (2) must be modified to account for an incomplete B-type phase transition. A more robust approach to accurately model the phase fractions and extract meaningful parameters is to use the following rate equation:
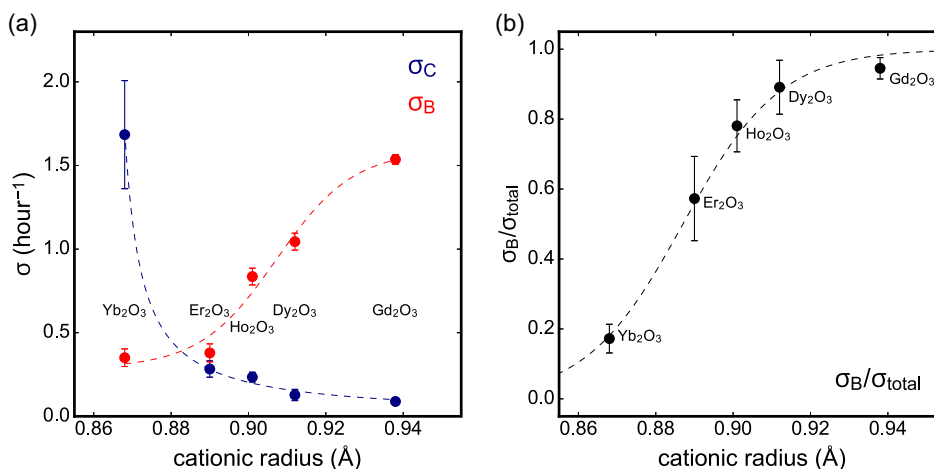
$$\frac{df_B}{dt} = \sigma_B(1 - f_B) - \sigma_C(f_B) \tag{3}$$

where the first term resembles Equation (1), which includes a term expressing the rate of B-type phase formation (σ_B). In addition, Equation (3) includes a second term modeling a reverse transformation of the B-type to the C-type phase, which is governed by a second transformation rate (σ_C) and the fraction of B-type phase available for this back-transformation (f_B). This is a simple correction to the direct-impact model that describes the phase behavior in a chemically and physically sensible manner. The solution to this equation for the B-type phase fraction as a function of milling time t is:

$$f_B(t) = \frac{\sigma_B\left(1 - e^{-(\sigma_B + \sigma_C)t}\right)}{\sigma_B + \sigma_C} \tag{4}$$

which collapses to the direct-impact model, with a complete transformation at high t, in the case of $\sigma_C = 0$. This equation was fit to the experimentally determined B-type phase fractions of each sesquioxide (dashed lines in Figure 4) and σ_B and σ_C extracted (**Figure 6**). The larger the slope of the initial linear increase ($f'_B(0) = \sigma_B$), the more rapidly the B-type phase forms in the mill (larger σ_B), while the lower the saturation level of the B-type phase ($f_B(\infty) = \sigma_B/[\sigma_B + \sigma_C]$), the more efficient the back transformation to the C-type phase is (larger σ_C and/or smaller σ_B).

In the case of ion irradiation, phase transitions are usually represented as a function of the ion fluence (ions/area) and σ has areal dimensions (cross-section). In the case of milling, duration is the key processing variable, such that σ_B and σ_C are expressed here as transformation rates (dimension of inverse time). Ion fluence is proportional to irradiation time (at constant

**ADVANCED
SCIENCE NEWS**

www.advancedsciencenews.com

**ADVANCED
ENGINEERING
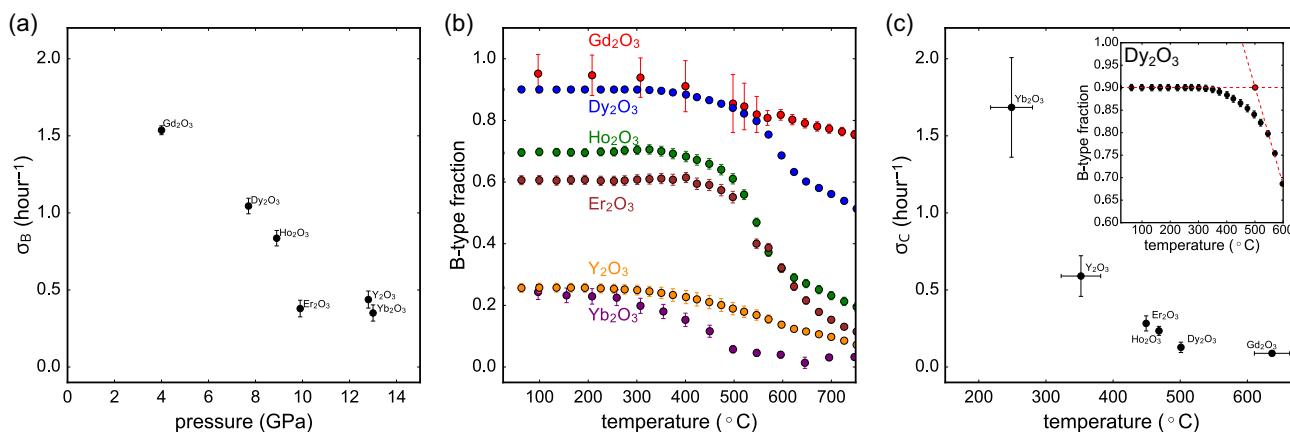MATERIALS**

www.aem-journal.com

Figure 6. Results of the fit of Equation (4) to the B-type phase fractions for each of the sesquioxides. Plotted against the cationic radius of each sesquioxide are: a) the extracted rate parameters σ_B and σ_C and b) the ratio of σ_B to the sum of σ_B and σ_C. Error bars correspond to the uncertainties of the function fitting. The dashed lines are to guide the eye.

flux), which is like milling time, proportional to the number of interactions and the accumulation of kinetic energy. Thus, the (modified) direct-impact behavior observed here suggests that each interaction between sample and milling tool directly results in a C-to-B-type phase transition within each impact region. However, the parameter σ_C suggests that some fraction of B-type transitions to the C-type equilibrium phase at ambient conditions.

The rate parameter σ_B generally increases with cationic radius (Figure 6a), similar to the σ_B parameter in the case of ion irradiation,[25] which is in good qualitative agreement to the initial linear fits of the B-type phase growth rate (Figure 5a). The behavior over the lanthanide series has a sigmoidal-like trend with cationic radius. In contrast, the rate of the reverse B-to-C-type phase transition (σ_C) is significantly larger for Yb_2O_3 than for the other sesquioxides and decreases with an exponential behavior for increasing cationic radii. The ratio of σ_B to the sum of both rates σ_B and σ_C (Figure 6b) yields the B-type phase saturation fraction and is in qualitative agreement with Figure 5b. The σ_B/σ_{total} ratio shows a sigmoid-like behavior in the milling process, and can be used to predict the two boundary sesquioxide compositions for which either no B-type phase will form under the present milling conditions (Lu_2O_3, $r_{Lu} = 0.861$ Å) or the transformation will proceed to completion (Sm_2O_3, $r_{Sm} = 0.958$ Å). This agrees well with the equilibrium temperature phase diagram (Figure 1) which shows that Sm_2O_3 can be readily synthesized as monoclinic B-type even at room temperature, while this high-temperature phase is inaccessible for Lu_2O_3. For even larger cations (e.g., Nd, $r_{Nd} = 0.983$ Å), M_2O_3 sesquioxides form other phases (A-type and H-type) and do not exhibit either C- or B-type structures from room temperature up to their melting points.

To better understand the underlying processes related to the transformation rates σ_B and σ_C and phase behavior in milled sesquioxides, we compare these parameters with the corresponding pressure and temperature phase diagrams. It has been shown before that all C-type structured sesquioxides transform to the

B-type phase under high pressure[24,25] with critical transition pressures that decrease with temperature. Like the pressure-induced C-to-B-type transformations, the B-type phase is apparent in all studied milled sesquioxides, with a nonzero σ_B rate across all samples evaluated. Therefore, this parameter may be linked to pressure-induced effects during the sample and milling tools. This is supported by the clear relation of σ_B with previously reported critical C-to-B transformation pressures across the sesquioxide compositional series, above which B-type starts to form at room temperature (**Figure 7**a).[24,25,46,47,59–62] If the milling process involves a certain (transient) pressure, the B-type formation rate goes down with an increasing critical phase transition pressure, as has been shown to accompany smaller cation sizes in prior (static) high-pressure experiments (with the important exception of Y_2O_3).[24,25] While the critical transition pressure increases generally with decreasing cationic radius, an exception is the behavior of Y_2O_3,[24,25] which shows a behavior similar to that of Yb_2O_3, despite having a cationic radius that is more comparable to Ho_2O_3. The B-type phase accumulation of milled Yb_2O_3 and the associated σ_B rate agrees very well with this behavior (Figure 6a), which demonstrates that the cationic radius alone is not the only parameter governing C-to-B-type transformation related to pressure (either static or dynamic). Based on the correlation of σ_B with the critical (static) pressure for B-type formation across all sesquioxides evaluated, and assuming that dynamic pressure effects do not noticeable differ from static compression, it can be estimated that milling in a planetary ball mill using tungsten carbide tools and a rotational speed of 350 rpm, may exert (transient) pressures in excess of 13 GPa, the C-to-B-type critical pressure for Yb_2O_3. Shear and frictional forces, however, can lower the critical pressure required for phase transformation compared to pure compression. For instance, plastic strain effectively reduces the kinetic barrier for nucleating new phases under high pressure. As mentioned above, the incomplete B-type phase formation under milling, particularly for sesquioxides with smaller cations (e.g., Yb_2O_3), suggests that additional processes are active during or after

ADVANCED
SCIENCE NEWS
www.advancedsciencenews.com

ADVANCED
ENGINEERING
MATERIALS
www.aem-journal.com

Figure 7. a) The σ_B rate parameter plotted against the previously established C-to-B transition pressures. Error bars represent uncertainties arising from the averaging of multiple datasets in literature. b) B-type phase fractions obtained from Rietveld refinement of XRD patterns collected in situ during temperature treatment, where error bars correspond to uncertainties from the refinement. c) The σ_C parameter plotted against the experimental determination of the onset temperature of B-C-type recovery. Inset in (c) shows a representative example of how this temperature is defined. The error bars represent the uncertainties from the Rietveld refinement of the B-type phase fraction.

milling that cause some back-transformation to C-type. Even if the rate of formation is low, continuous milling over extended time frames would eventually lead to a complete transformation; thus, the recovery of the C-type phase must continuously occur with milling time, the rate of which is best described by the parameter σ_C.

To gain further insight into the phase transition behavior, we performed in situ high-temperature XRD experiments on previously-milled sesquioxides that had reached a steady state saturation regime of the B-type fraction with a mixture of B- and C-type phases. Each compound was fully transformed back to the C-type phase with increasing temperature (Figure 7b) with the exception of Gd_2O_3 which, after partially transforming back to C-type, transformed fully to B-type at the highest temperatures, in agreement with the temperature phase diagram (Figure 1). In each case, the B- and C-type phase fractions remained constant upon heating up to a critical temperature above which the B-type phase fraction decreased with a near-linear trend with further increase in temperature. To approximate the C-type recovery onset temperature of each sesquioxide, two linear regressions were fit to the B-type fractions: 1) a horizontal line through the steady-state region at low temperatures (i.e., a line with slope zero and y-intercept equal to the steady-state fraction) and 2) a line through the decreasing linear trend after the onset of C-type recovery. The intersection of these two lines was defined as the onset temperature of C-type recovery and was plotted against the σ_C parameter (Figure 7c). This comparison reveals that the rate σ_C generally captures the behavior of the recovery temperatures: sesquioxides with lower C-type recovery temperatures have high σ_C parameters and vice versa. This indicates that the recovery process is thermally activated and the derived σ_C describes this process. Similar to the comparison between σ_B and pressure over the compositional range, we can estimate, based on the correlation of σ_C with the onset of C-type recovery temperature, that milling with a planetary ball mill under the present conditions induces temperatures in excess of 630 °C, the recovery temperature of Gd_2O_3. While

high-temperature conditions may lower the transition pressure and aid the formation of the B-type phase, thermal effects appear to be the key driver for the back-transformation to C-type. Taking into account the hot spot and magma-plasma models, this temperature regime is highly transient.[1]

Pressure effects play the dominant role in the C-to-B-type phase transition during the milling process. This becomes further apparent when comparing the structural pathway with that induced by swift heavy ion irradiation. Previous irradiation experiments coupled with synchrotron XRD demonstrated that the B-type phase (40-2) diffraction maxima[27] are disproportionately intense in the patterns of irradiated sesquioxides (**Figure 8**a). This differs clearly from the XRD diffraction patterns of the milled B-type phase that are dominated by the (310) peaks (Figure 8b). Tracy et al.[27] hypothesized that the disproportionately intense (40-2) peak originates from local nucleation of the B-type phase via anion Frenkel defects in the C-type phase (displacement of 48e anions to the 16c vacancies in adjacent planes). This anion defect-driven process is accompanied by crystallographic shear, and ultimately the dissolution of every fourth (222)$_C$ anion plane, leading to three fully dense anion planes (¾ + ¾ + ¾ + ¾ = 1 + 1 + 1) and fully dense Ising triangular nets (**Figure 9**).[18,19] With increasing irradiation, oxygen anti-Frenkel defects accumulate and rearrange in C-type sesquioxides, producing fully dense anion planes characteristic of the (40-2)$_B$ anion planes. At higher fluences, this eventually leads to a complete transformation to the B-type structure. Since sesquioxides are oxygen conductors at high temperatures, the occurrence of intense diffraction maxima characteristic of anion defects may be an indicator of a more thermally driven C-to-B phase transition in the case of extremely ionizing swift heavy ions.

In clear contrast, the intense (310)$_B$ peak in the milled B-type phase (Figure 8b) is more in agreement with a pressure/stress-driven phase transition that proceeds via the cation sublattice. The {100} cation planes in the C-type phase are fully dense square atomic nets[19] (Figure 9), and therefore most susceptible
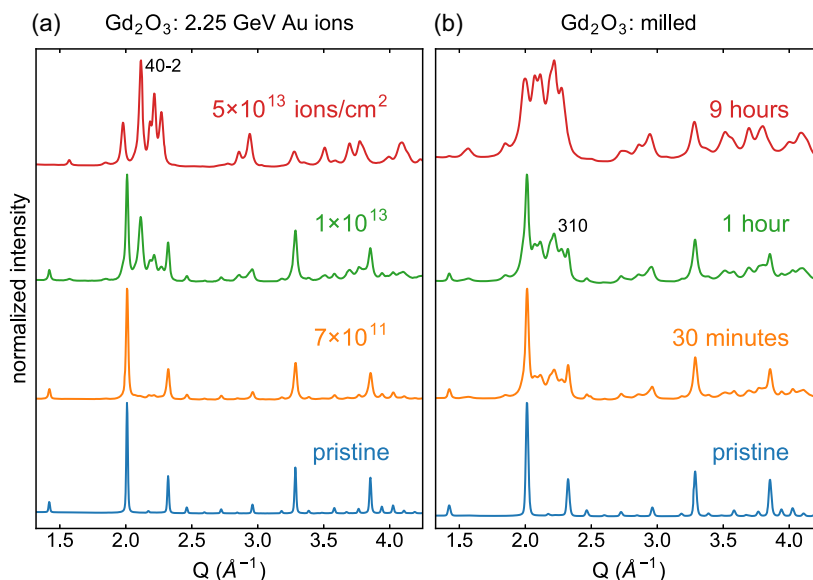
Figure 8. a) Comparison of XRD patterns collected from Gd_2O_3 prepared by high-energy ion irradiation and b) high-energy ball milling. In each case, disproportionately intense maxima are labeled: (40-2) for the ion irradiation Gd_2O_3 and (310) for the milled Gd_2O_3. Data in (a) from are taken Tracy et al. (ref. [27]).
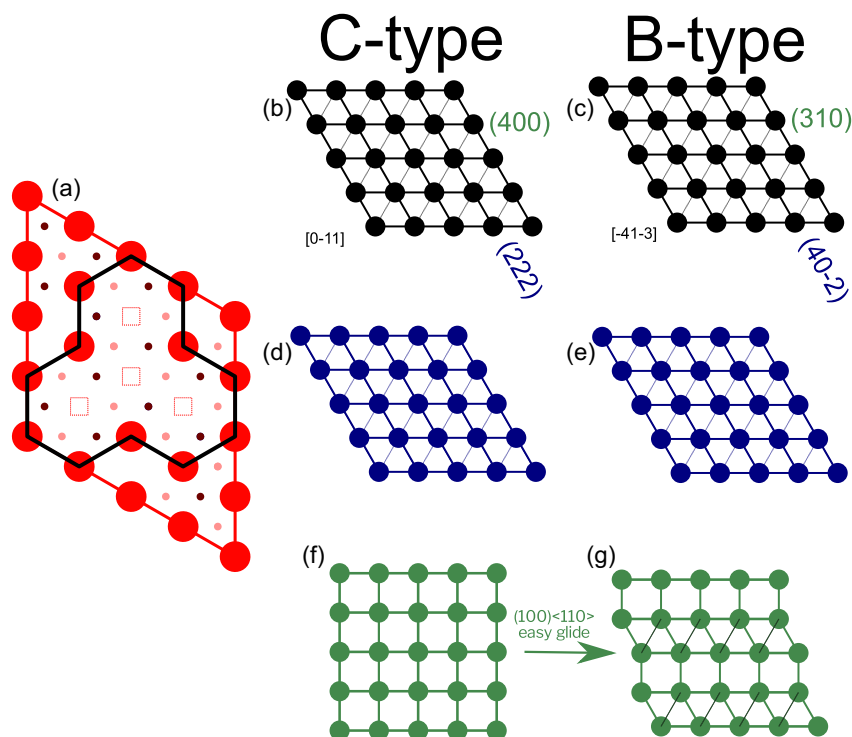
Figure 9. Structural relation between the cubic "C-type" and monoclinic "B-type" Ln_2O_3 phases. a) The oxygen sublattice of the "C-type" phase exhibits a wishbone-shaped cluster of vacancies which does not exist in the "B-type" phase. b,c) Analogous viewing directions of cation sublattice in the two phases and comparison of two sets of planes. d) The $(222)_C$ planes and e) $(40\text{-}2)_B$ are both dense triangular nets of cations. f,g) The $(400)_C$ planes are square nets of cations which are susceptible to slip systems which locally nucleate $(310)_B$ planes.

to slip.[20] Plastic deformation of C-type structures has been shown to proceed in high-stress fields in the (001)⟨110⟩ glide slip system.[63] This is a rather simple slip system that involves

homogeneous shear of 30° that converts a square net to a hexagonal net (Figure 9). The variation of the $(100)_C$ ideal square net through this slip system will nucleate $(310)_B$ cation planes and

**ADVANCED
SCIENCE NEWS**
www.advancedsciencenews.com

**ADVANCED
ENGINEERING
MATERIALS**
www.aem-journal.com

give rise to a disproportionately intense diffraction peak.[64] This suggests that the formation of the B-type phase proceeds through different crystallographic mechanisms when comparing the two far-from-equilibrium processing techniques.

Based on the formation of the high-pressure/temperature B-type M_2O_3 phases, we conclude that high-energy ball milling and irradiation with swift heavy ions involve highly transient pressure and temperature regimes. Based on the structural pathway followed and on the correlation to pressure/temperature phase diagrams, it becomes apparent that compression plays a more dominant role during milling with a planetary ball mill and temperature during irradiation with swift heavy ions. The inelastic thermal-spike model has been developed for swift heavy ion irradiation to describe the formation of ion tracks and other structural modifications resulting from electronic interactions which result in rapid heating and quenching processes.[65–77] In this model, energy from the bombarding ion is first deposited to and shared among the target electrons. Then, through electron–phonon coupling, the energy is transferred to the lattice which rapidly induces a large increase in temperature. The premise, going back to the original formulation by Seitz and Koehler in 1956,[69,72] is that in this nanometric high-temperature region, which forms less than one picosecond after ion impact, the temperature can rise above the melting point of the material, reaching local temperatures in excess of 10 000 K.[67,78,79] These thermal spikes can generate large pressure waves caused by the rapid expansion of heated material reaching up to tens of GPa.[68,80]

Our data confirm that elevated temperature and pressure also play key roles in ball milling. Initially, the "hot-spot theory" proposed that extreme temperatures of over 1000 K are reached over an interaction area of $\approx 1\,\mu m^2$ during a milling event, such as ball–ball impacts. Indeed, this was later experimentally confirmed for a few materials, including quartz, for which the temperature at a propagating crack was estimated to be several thousand K.[7,81] According to the first proposed comprehensive model, the "Magma-Plasma model," local temperatures at the surface of colliding particles can reach in excess of 10 000 K[5,7,8] which induces a physical state consistent with a "triboplasma," a form of highly ionized gas generated by the sliding contact of two solids.[82] The subsequent relaxation of the excited triboplasmatic state leads to the emission of excited solid fragments, electrons, and photos are emitted over millisecond time frames.[83] This excited state is so short-lived that a temperature cannot be ascribed, and the stochastic chemical processes occurring during this material phase cannot be explained with the laws of equilibrium thermodynamics.[8] It has been reported that such extremes can also induce conditions up to 17 GPa through transient applications of hydrostatic pressure and displacive shear pressure.[2,84]

Our data, particularly the saturation of the milling-induced B-type phase below unity, align closely with previous high-pressure torsion (HPT) experiments. This alignment is evident in the competition between pressure-induced phase transition processes and thermally activated recovery processes, which prevent complete conversion and result in partial transformations. These transformations reach steady states, where the phase fraction under a given set of milling parameters depends on the specific chemical compound. This behavior is consistent with work on ZrO_2, where powder particles achieved a steady state between the tetragonal and monoclinic forms due to conditions within the ball mill similar to those in HPT.[85] Although there is limited literature on HPT studies specifically on lanthanide sesquioxides (Ln_2O_3), recent work on Y_2O_3[86] reported a mixture of monoclinic and cubic phases obtained by HPT, which is consistent with our findings. Additional, other factors may contribute to the mixed-phase character of our milled samples. For instance, a study on Al_2O_3[87] found that the pure γ-alumina phase remained stable and did not transform, even after extended milling. However, when a small amount of α-alumina was present during milling, γ-alumina gradually transformed into α-alumina, suggesting a nucleation and growth mechanism driven by the presence of α-alumina seeds. In our case, the incomplete conversion to the B-phase may indicate that the remaining C-phase similarly aids in the recovery of the C-phase. These insights underscore the complex interplay of mechanochemical processes and the opportunity to deepen our understanding of the fundamental mechanisms driving polymorphic transformations under far-from-equilibrium conditions.

Interestingly, for both ion irradiation and ball milling, deposited energy generally exhibits a strong spatial gradient which decreases in intensity radially outward from the center of the interaction zone. This energy-deposition profile has been used to explain complex damage morphologies within ion tracks that often consist of concentric damage zones with different effects, such as cores, shells, and halos.[58,88] Core-shell type damage behavior has been also reported in ball-milled materials[89] and this can also explain the incomplete B-type phase transformation in sesquioxides. In the core zone of interaction, both pressure and temperature may exceed the critical values to trigger rapidly the C-to-B transformation, while in a shell region elevated temperatures during quenching may convert some of the B-type phase back to the equilibrium C-type phase.

Kinematic modeling of far-from-equilibrium processes can yield additional insight into the extreme conditions present during the transient energy deposition. Modeling sample tool interactions within a mill is complex and involves determining the velocity of a ball launched against jar walls during the rotation of the disc and the jars.[90–93] The kinetic energy of a ball before and after impact is a crucial parameter that depends on ball mass, velocity, and the elasticity of the collision. Operation with multiple balls requires a yield coefficient to account for the impeding of ball velocity by other balls.[90] The collision frequency depends on rotational speed and the number of balls, which affects the final energy imparted to the sample during milling. In this work, the deposited energy was estimated using an approach introduced by Kessler and Rinaldi,[91] given by:

$$\text{Energy dose}\left[\frac{\text{Energy}}{\text{Mass}}\right] = \varphi_b N_b m_b t \omega_P^3 \left(R_J - \frac{d_b}{2} + R_P \right) \frac{\left(R_J - \frac{d_b}{2} \right)}{\pi W} \tag{5}$$

where φ_b is a yield coefficient accounting for energy dissipation in the case of multiple balls, N_b is the number of balls, m_b is the mass per ball, t is the milling duration, ω_p is the absolute angular velocity of the milling plate, R_J is the grinding jar radius, d_b is the diameter of the balls, R_P is the radius of the milling plate, and W is the mass of the sample. By contrast, the energy dose deposited into the sample by ion irradiation is given by:
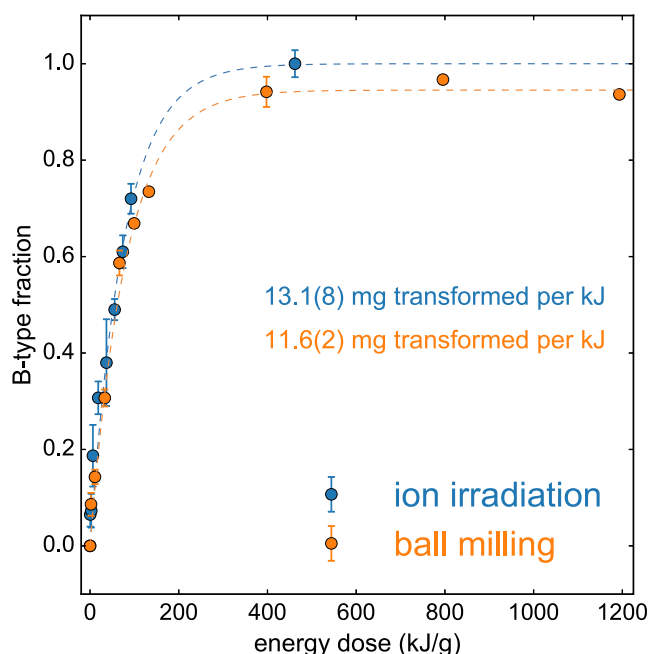
Figure 10. Accumulation of monoclinic "B-type" structure in Gd_2O_3 induced by 2.25 GeV Au ions (blue) and ball milling at 350 rpm with WC tools (orange) as a function of energy deposited into the sample. The orange and blue dashed lines are fits of the Equation (5) and (6), respectively, to the data points.

$$\text{Energy dose} \left[\frac{\text{Energy}}{\text{Mass}} \right]$$

$$= \frac{\frac{dE}{dx} \, [\text{Energy loss per ion per path length}]}{\rho \, [\text{Mass per volume}]} \phi \, [\text{Ions per area}] \qquad (6)$$

where dE/dx is the energy loss per path length ("stopping power") of the ion in the material, ϕ is the ion fluence, and ρ is the material density. A comparison of the energetics of the C-to-B-type phase transformation induced in Gd_2O_3 was made between milling, in this study, and by ion irradiation, from the data in Tracy et al.[27] The B-type fractions obtained from Rietveld refinement (Figure 4) were then compared with the corresponding energy dose. Remarkably, despite the difference in both processing techniques, such as the duration and length-scale of interaction, the amount of B-type phase formed *per* unit energy dose is very similar (**Figure 10**). Further, the B-type fraction can be evaluated using Equation (5) (ions) and 6 (milling) to extract the mass of B-type phase produced per energy deposition (13.1(8) mg kJ^{-1} for ions and 11.6(2) mg kJ^{-1} for milling). This energetic consideration is strongly dependent on ion species, ion velocity, ion flux, milling tool, milling speed, sample-to-ball ratio, and for this study, those parameters were such that they resulted in very similar transformation rates per unit energy deposited, even though the sample undergoes complete transformation to the B-phase under radiation but not under milling.

4. Conclusion

The cubic-to-monoclinic C-to-B-type phase transformation in binary sesquioxides (M_2O_3, M = Gd, Dy, Ho, Er, Yb, and Y) was used to gain further insight into the transient extremes that occur during the milling process. All sesquioxides show transformation to the B-type phase after milling, but the formation rate and maximum attainable phase fraction are strongly correlated with the radius of the lanthanide cation. None of the sesquioxides exhibited 100% B-type phase even after extended milling times. Instead, the phase fractions reach a steady state level that increases with the size of the cation. This suggests some recovery process during milling that transforms the B-type phase back to the initial C-type phase. Using a rate theory approach, two parameters were extracted that describe both the B-type formation rate (σ_B) and C-type recovery rate (σ_C). The parameter σ_B scales closely with the critical phase transformation pressure from previous static-pressure experiments, while in situ annealing studies of milled samples suggest that σ_C is related to thermally-driven recovery process. The B-type phase formation in sesquioxides was compared with transformations induced by swift heavy ions. Based on XRD patterns and texture effects with increasing radiation fluence or milling time, it can be concluded that the accumulation of anion Frenkel defects plays an important role in the structural transformation to the B-type phase under ion irradiation, indicative of thermally driven effects. In contrast, XRD patterns and distinct texture effects show that the C-to-B-type transformation proceeds via slip systems in cation planes within the ball mill indicative of pressure-driven effects. While in both far-from-equilibrium processing technique transient pressure and temperature play a key role, their importance is reversed in ball milling as compared to swift heavy ions. Based on the behavior of σ_B and σ_C across the sesquioxide series and relation to the known effects of (static) pressure and temperature conditions it was estimated that under the current milling conditions at 350 rpm, transient regimes of over 13 GPa and 630 °C are reached. Finally, the B-type formation induced by ions and ball milling is kinematically modeled and it is shown that the amount of material transformed per energy dose is similar for both processing methods. Further studies should focus on a wide range of ball milling and ion irradiation conditions, and a comparison of energy deposited in the system with experimental calorimetric data should be performed to evaluate the energy stored in the system.

Conflict of Interest

The authors declare no conflict of interest.

Data Availability Statement

The data that support the findings of this study are available from the corresponding author upon reasonable request.

Keywords

[1] V. Šepelák, S. Bégin-Colin, G. Le Caër, *Dalt. Trans.* **2012**, *41*, 11927.

[2] P. Baláž, M. Achimovičová, M. Baláž, P. Billik, Z. Cherkezova-Zheleva, J. M. Criado, F. Delogu, E. Dutková, E. Gaffet, F. J. Gotor, R. Kumar, I. Mitov, T. Rojac, M. Senna, A. Streletskii, K. Wieczorek-Ciurowa, *Chem. Soc. Rev.* **2013**, *42*, 7571.

[3] C. Suryanarayana, *Prog. Mater. Sci.* **2001**, *46*, 1.

[4] C. Suryanarayana, E. Ivanov, V. V. Boldyrev, *Mater. Sci. Eng. A* **2001**, *304–306*, 151.

[5] P. A. Thiessen, K. Meyer, G. Heinicke, *Grundlagener Tribochemie*, Akademie-Verlag, Berlin **1967**.

[6] F. P. Bowden, A. D. Yoffe, G. E. Hudson, *Am. J. Phys.* **1952**, *20*, 250.

[7] P. Baláž, *Mechanochem. Nanosci. Miner. Eng.* **2008**, 1.

[8] L. Takacs, *Chem. Soc. Rev.* **2013**, *42*, 7649.

[9] R. T. O'Neill, R. Boulatov, *Nat. Rev. Chem.* **2021**, *5*, 148.

[10] M. Hong, J. Kwo, A. R. Kortan, J. P. Mannaerts, A. M. Sergent, *Science* **1999**, *283*, 1897.

[11] L. Zhou, Z. Gu, X. Liu, W. Yin, G. Tian, L. Yan, S. Jin, W. Ren, G. Xing, W. Li, X. Chang, Z. Hu, Y. Zhao, *J. Mater. Chem.* **2012**, *22*, 966.

[12] M. Durazzo, F. B. V. Oliveira, E. F. Urano De Carvalho, H. G. Riella, *J. Nucl. Mater.* **2010**, *400*, 183.

[13] V. M. Goldschmidt, *J. Chem. Soc.* **1937**, 655.

[14] W. Zachariasen, *Nor. Geol. Tidsskr.* **1927**, *9*, 310.

[15] L. Pauling, M. D. Shappell, *Z. Fur Krist. - Cryst. Mater.* **1930**, *75*, 128.

[16] F. J. Manjón, J. A. S. Tresserras, J. Ibáñez, A. L. J. Pereira, *Crystals* **2019**, *9*, 630.

[17] T. D. Chikalla, C. E. McNeilly, F. P. Roberts, *J. Am. Ceram. Soc.* **1972**, *55*, 428.

[18] B. P. Uberuaga, K. E. Sickafus, *Comput. Mater. Sci.* **2015**, *103*, 216.

[19] G. H. Wannier, *Phys. Rev.* **1950**, *79*, 357.

[20] K. E. Sickafus, R. W. Grimes, S. M. Corish, A. R. Cleave, M. Tang, C. R. Stanek, B. P. Uberuaga, J. A. Valdez, *Layered Atom Arrangements in Complex Materials*, United States **2005**.

[21] M. Foex, J. P. Traverse, *Rev. Int. Hautes Temp. Refract.* **1966**, *3*, 429.

[22] J. Coutures, M. Foex, *J. Solid State Chem.* **1974**, *11*, 294.

[23] J. Coutures, A. Rouanet, R. Verges, M. Foex, *J. Solid State Chem.* **1976**, *17*, 171.

[24] M. Zinkevich, *Prog. Mater. Sci.* **2007**, *52*, 597.

[25] H. R. Hoekstra, *Inorg. Chem.* **1966**, *5*, 754.

[26] G. Sattonnay, S. Bilgen, L. Thomé, C. Grygiel, I. Monnet, O. Plantevin, C. Huet, S. Miro, P. Simon, *Phys. Status Solidi Basic Res.* **2016**, *253*, 2110.

[27] C. L. Tracy, M. Lang, F. Zhang, C. Trautmann, R. C. Ewing, *Phys. Rev. B* **2015**, *92*, 174101.

[28] S. Hémon, V. Chailley, E. Dooryhée, C. Dufour, F. Gourbilleau, F. Levesque, E. Paumier, *Nucl. Instrum. Methods Phys. Res. Sect. B* **1997**, *122*, 563.

[29] A. P. Solomon, C. L. Tracy, E. C. O'Quinn, D. Severin, M. K. Lang, *J. Appl. Phys.* **2021**, *129*, 225903.

[30] N. Li, S. K. Yadav, Y. Xu, J. A. Aguiar, J. K. Baldwin, Y. Q. Wang, H. M. Luo, A. Misra, B. P. Uberuaga, *Sci. Rep.* **2017**, *7*, 40148.

[31] V. Kocevski, J. A. Valdez, B. K. Derby, Y. Q. Wang, G. Pilania, B. P. Uberuaga, *Mater. Adv.* **2023**, *4*, 1101.

[32] C. Suryanarayana, *Research* **2024**, *2019*, 4219812.

[33] V. Šepelák, A. Düvel, M. Wilkening, K. D. Becker, P. Heitjans, *Chem. Soc. Rev.* **2013**, *42*, 7507.

[34] G. Garcia-Martinez, L. G. Martinez-Gonzalez, J. I. Escalante-García, A. F. Fuentes, *Powder Technol.* **2005**, *152*, 72.

[35] A. F. Fuentes, K. Boulahya, M. Maczka, J. Hanuza, U. Amador, *Solid State Sci.* **2005**, *7*, 343.

[36] M. Lang, C. L. Tracy, R. I. Palomares, F. Zhang, D. Severin, M. Bender, C. Trautmann, C. Park, V. B. Prakapenka, V. A. Skuratov, R. C. Ewing, *J. Mater. Res.* **2015**, *30*, 1366.

[37] C. Prescher, V. B. Prakapenka, *High Press. Res.* **2015**, *35*, 223.

[38] G. Ashiotis, A. Deschildre, Z. Nawaz, J. P. Wright, D. Karkoulis, F. E. Picca, J. Kieffer, *J. Appl. Crystallogr.* **2015**, *48*, 510.

[39] B. H. Toby, R. B. Von Dreele, *J. Appl. Crystallogr.* **2013**, *46*, 544.

[40] H. M. Rietveld, *J. Appl. Crystallogr.* **1969**, *2*, 65.

[41] A. March, *Z. Für Krist. Mater.* **1932**, *81*, 285.

[42] W. A. Dollase, *J. Appl. Crystallogr.* **1986**, *19*, 267.

[43] N. Dilawar Sharma, J. Singh, A. Vijay, K. Samanta, S. Dogra, A. K. Bandyopadhyay, *J. Phys. Chem. C* **2016**, *120*, 11679.

[44] G. Kimmel, R. Z. Shneck, W. Lojkowski, Z. Porat, T. Chudoba, D. Mogilyanski, S. Gierlotka, V. Ezersky, J. Zabicky, *J. Am. Ceram. Soc.* **2019**, *102*, 3829.

[45] I. F. Ferguson, *Acta Crystallogr. A* **1975**, *31*, S69.

[46] T. Atou, K. Kusaba, K. Fukuoka, M. Kikuchi, Y. Syono, *J. Solid State Chem.* **1990**, *89*, 378.

[47] C. Meyer, J. P. Sanchez, J. Thomasson, J. P. Itié, *Phys. Rev. B* **1995**, *51*, 12187.

[48] G. Martin, P. Bellon, *Solid State Phys. Adv. Res. Appl.* **1996**, *50*, 189.

[49] M. Lang, F. Djurabekova, N. Medvedev, M. Toulemonde, C. Trautmann, *Comprehensive Nuclear Materials*, Vol. 1, Elsevier, Amsterdam **2020**, pp. 485–516.

[50] C. Gibert-Mougel, F. Couvreur, J. M. Costantini, S. Bouffard, F. Levesque, S. Hémon, E. Paumier, C. Dufour, *J. Nucl. Mater.* **2001**, *295*, 121.

[51] M. Lang, F. Zhang, J. Zhang, J. Wang, J. Lian, W. J. Weber, B. Schuster, C. Trautmann, R. Neumann, R. C. Ewing, *Nucl. Instrum. Methods Phys. Res. Sect. B* **2010**, *268*, 2951.

[52] G. Sattonnay, C. Grygiel, I. Monnet, C. Legros, M. Herbst-Ghysel, L. Thomé, *Acta Mater.* **2012**, *60*, 22.

[53] M. Lang, R. Devanathan, M. Toulemonde, C. Trautmann, *Curr. Opin. Solid State Mater. Sci.* **2015**, *19*, 39.

[54] N. Itoh, D. M. Duffy, S. Khakshouri, A. M. Stoneham, *J. Phys. Condens. Matter* **2009**, *21*, 474205.

[55] F. F. Komarov, *Physics-Uspekhi* **2017**, *60*, 435.

[56] J. Zhang, M. Lang, R. C. Ewing, R. Devanathan, W. J. Weber, M. Toulemonde, *J. Mater. Res.* **2010**, *25*, 1344.

[57] J. F. F. Gibbons, *Proc. IEEE* **1972**, *60*, 1062.

[58] E. C. O'Quinn, C. L. Tracy, W. F. Cureton, R. Sachan, J. C. Neuefeind, C. Trautmann, M. K. Lang, *J. Mater. Chem. A* **2021**, *9*, 16982.

[59] Y. Zhang, I. H. Jung, *Calphad Comput. Coupling Phase Diagrams Thermochem.* **2017**, *58*, 169.

[60] L. Bai, J. Liu, X. Li, S. Jiang, W. Xiao, Y. Li, L. Tang, Y. Zhang, D. Zhang, *J. Appl. Phys.* **2009**, *106*, 1.

[61] S. Jiang, J. Liu, X. Li, L. Bai, W. Xiao, Y. Zhang, C. Lin, Y. Li, L. Tang, *J. Appl. Phys.* **2011**, *110*, 13526.

[62] Q. Guo, Y. Zhao, C. Jiang, W. L. Mao, Z. Wang, J. Zhang, Y. Wang, *Inorg. Chem.* **2007**, *46*, 6164.

[63] M. Boisson, R. J. Gaboriaud, *J. Mater. Sci.* **1981**, *16*, 3452.

[64] M. O'Keeffe, B. G. Hyde, *Philos. Trans. R. Soc. London. Ser. A* **1980**, *295*, 553.

[65] G. Szenes, *Radiat. Meas.* **1995**, *25*, 39.

[66] G. Szenes, *Nucl. Instrum. Methods Phys. Res. Sect. B* **1996**, *116*, 141.

[67] M. Toulemonde, C. Dufour, A. Meftah, E. Paumier, *Nucl. Instrum. Methods Phys. Res. Sect. B* **2000**, *166*, 903.

[68] A. Norman, *Radiat. Res. Suppl.* **1967**, *7*, 33.

[69] F. Seitz, J. Koehler, *Solid State Phys.* **1956**, *2*, 307.

[70] M. Toulemonde, W. J. Weber, G. Li, V. Shutthanandan, P. Kluth, T. Yang, Y. Wang, Y. Zhang, *Phys. Rev. B - Condens. Matter Mater. Phys.* **2011**, *83*, 1.

[71] C. Trautmann, M. Toulemonde, K. Schwartz, J. M. Costantini, A. Müller, *Nucl. Instrum. Methods Phys. Res. Sect. B* **2000**, *164*, 365.

[72] T. Wiss, H. Matzke, C. Trautmann, M. Toulemonde, S. Klaumünzer, *Nucl. Instrum. Methods Phys. Res. Sect. B* **1997**, *122*, 583.

[73] C. Trautmann, M. Toulemonde, C. Dufour, E. Paumier, *Nucl. Instrum. Methods Phys. Res. Sect. B* **1996**, *108*, 94.

[74] M. Toulemonde, W. Assmann, C. Dufour, A. Meftah, F. Studer, C. Trautmann, *Ion Beam Science:Solved and Unsolved Problems*, The Royal Danish Academy of Sciences and Letters, Copenhagen, Denmark, **2006**, pp. 263–292.

[75] P. Kluth, C. S. Schnohr, O. H. Pakarinen, F. Djurabekova, D. J. Sprouster, R. Giulian, M. C. Ridgway, A. P. Byrne, C. Trautmann, D. J. Cookson, K. Nordlund, M. Toulemonde, *Phys. Rev. Lett.* **2008**, *101*, 1.

[76] M. Toulemonde, E. Paumier, C. Dufour, *Radiat. Eff. Defects Solids* **1993**, *126*, 201.

[77] H. M. Naguib, R. Kelly, *Radiat. Eff.* **1975**, *25*, 1.

[78] A. V. Lankin, I. V. Morozov, G. E. Norman, S. A. Pikuz, I. Y. Skobelev, *Phys. Rev. E - Stat. Nonlinear, Soft Matter Phys.* **2009**, *79*, 1.

[79] G. E. Norman, S. V. Starikov, V. V. Stegailov, I. M. Saitov, P. A. Zhilyaev, *Contrib. Plasma Phys.* **2013**, *53*, 129.

[80] N. Medvedev, A. E. Volkov, R. Rymzhanov, F. Akhmetov, S. Gorbunov, R. Voronkov, P. Babaev, *J. Appl. Phys.* **2022**, *133*, 100701.

[81] R. Weichert, K. Schönert, *Chemie Ing. Tech.* **1976**, *48*, 543.

[82] K. Nakayama, in *Enciclopedya of Tribologia* (Eds: Q. J. Wang, Y.-W. Chung), Springer US, Boston, MA **2013**, p. 3750.

[83] C. Kajdas, in *Tribology in Enginering* (Ed: H. Pihtili), IntechOpen, Rijeka **2013**, Ch. 11.

[84] F. Delogu, *Phys. Rev. B* **2010**, *82*, 205415.

[85] F. Delogu, *Scr. Mater.* **2012**, *67*, 340.

[86] H. Razavi-Khosroshahi, K. Edalati, H. Emami, E. Akiba, Z. Horita, M. Fuji, *Inorg. Chem.* **2017**, *56*, 2576.

[87] Y. Wang, C. Suryanarayana, L. An, *J. Am. Ceram. Soc.* **2005**, *88*, 780.

[88] M. Lang, M. Toulemonde, J. Zhang, F. Zhang, C. L. Tracy, J. Lian, Z. Wang, W. J. Weber, D. Severin, M. Bender, C. Trautmann, R. C. Ewing, *Nucl. Instrum. Methods Phys. Res. Sect. B* **2014**, *336*, 102.

[89] A. F. Fuentes, L. Takacs, *J. Mater. Sci.* **2013**, *48*, 598.

[90] N. Burgio, A. Iasonna, M. Magini, S. Martelli, F. Padella, *Nuovo Cim. D* **1991**, *13*, 459.

[91] M. Kessler, R. Rinaldi, *Front. Chem.* **2022**, *9*, 1.

[92] S. Y. Lu, Q. J. Mao, Z. Peng, X. D. Li, J. H. Yan, *Chinese Phys. B* **2012**, *21*, 078201.

[93] V. V. Zyryanov, *Russ. Chem. Rev.* **2008**, *77*, 105.